UDK 661.862:620.193.4
Original scientific article/Izvirni znanstveni članek

ISSN 1580-2949
MTAEC9, 56(2)139(2022)

MICROSTRUCTURE EVOLUTION AND CORROSION BEHAVIOR OF Al-Si/Al-Mn COMPOSITES IN SALT SPRAY

RAZVOJ MIKROSTRUKTURE IN KOROZIJA KOMPOZITOV Al-Si/Al-Mn V SLANI KOMORI

Zhifeng Li[1,2]

[1]College of Mechanical and Electrical Engineering, Central South University, Changsha 410083, China
[2]State Key Laboratory of High Performance Complex Manufacturing, Central South University, Changsha 410083, China

Prejem rokopisa – received: 2022-01-03; sprejem za objavo – accepted for publication: 2022-02-02

doi:10.17222/mit.2022.354

Al-Si/Al-Mn composites are commonly used in aluminum heat exchangers. Improving their corrosion resistance is the key for prolonging their service life and reducing their costs. In this paper, an artificial salt spray corrosion test was adopted in accordance with the ASTM G85 standard to evaluate the atmospheric corrosion resistance of Al-Si/Al-Mn composites. The corroded samples were tested with electrochemical impedance spectroscopy (EIS). Microstructure evolution and their corrosion mechanism were discussed after the use of OM, SEM, EPMA and XRD. The results showed two corrosion mechanisms, including the pitting-induction mechanism and intergranular-development mechanism: pitting is induced by the destruction of the passive film as Cl^- is adsorbed at the defects, while the corrosive medium in the pitting pores expands along the grain boundaries where eutectic Si is enriched. A corrosion process can be divided into three periods: the pitting-induction period, pitting-propagation period and matrix-corrosion period. The equivalent circuit models established sequentially were consistent with the actual macroscopic and microscopic observations.

Key words: Al-Si/Al-Mn composites, salt spray, pitting corrosion, electrochemical impedance spectroscopy

Kompoziti na osnovi Al-Si/Al-Mn se uporabljajo za izdelavo toplotnih izmenjevalnikov. Za podaljšanje njihove življenjske dobe in znižanje cene je potrebno izboljšati njihovo odpornost proti koroziji. V članku avtorji opisujejo ovrednotenje atmosferske korozijske odpornosti izbranih kompozitov Al-Si/Al-Mn s pomočjo korozijskih preizkusov v skladu s standardom ASTM G85. Korodirane vzorce so nato testirali z elektro-kemijsko impedančno spektroskopijo (EIS) in jih mikrostrukturno okarakterizirali s pomočjo optičnega (OM) in vrstičnega elektronskega mikroskopa (SEM). Razvoj korozijskega mehanizma so ovrednotili tudi s pomočjo mikrokemijskih analiz na elektronski mikro sondi (EMPA; Electron Micro Probe Analyzer) in rentgensko difrakcijsko spektroskopijo (XRD). V razpravi avtorji ugotavljajo, da prihaja do dveh mehanizmov korozije in sicer: jamičaste korozije in korozije na mejah med kristalnimi zrni. Nastanek korozijskih jamic inducira porušitev pasivnega filma zaradi adsorbcije Cl^- ionov na napakah v materialu. Korozijski medij nato prodira v korozijske jamice vzdolž kristalnih mej, kjer napada področja obogatena z evtektskim Si. Proces korozije so avtorji razdelili na tri časovna obdobja: začetek nastajanja jamic, napredovanje nastajanja jamic (povečevanje njihovega števila in velikosti) ter končno obdobje, ko prihaja še do korozije kovinske matice. Ugotovljeni odgovarjajoči krožni modeli zaporedja mehanizmov korozije se ujemajo z dejanskimi makroskopskimi in mikroskopskimi opazovanji.

Ključne besede: kompoziti Al-Si/Al-Mn, slana komora, jamičasta korozija, elektro-kemijska impedančna spektroskopija

1 INTRODUCTION

Heat exchangers play an important role in the chemical industry, petroleum industry, power industry, automotive industry, etc. Aluminum alloys have gradually replaced copper alloys as the main material for heat exchangers as they exhibit lower density and better corrosion resistance and they are also more environmentally friendly. Al-Si/Al-Mn composites are most widely used.[1] Al-Mn has excellent comprehensive properties as the matrix material, and Al-Si has a slightly lower melting point, leading to excellent brazing fluidity when used the external solder alloy. Many researchers are concerned about the heat-transfer performance, suggesting structural optimization and manufacturing improvement.[2–6] However, enhancing corrosion resistance is more important in order to avoid the perforation of closed pipes and pressure drop of the heat sinks for heat exchangers.[7]

Heat exchangers have to resist both medium corrosion and atmospheric corrosion.[8–11] Compared to medium corrosion, atmospheric corrosion is more complex, having a more changeable mechanism. Various studies focus on atmospheric corrosion. Chandra et al. investigated metallurgical changes and the mode of corrosion attack and type of corrosion products of a heat-exchanger tube.[12] Peltola et al. observed the ant-nest corrosion morphology of fin heat exchangers[13], while Nasrazadani et al. analyzed the phases of ant-nest corrosion products.[14] Kim et al. evaluated the multi-galvanic effect of Al finned-tube heat exchangers, using polarization tests, a numerical simulation and a sea water acetic acid test (SWAAT).[15] Su et al. pointed out that chloride damages the passive film and initiates corrosion.[16] Cho et al. discovered that corrosion behavior depended mainly on the concentrations of zinc, aluminum and oxygen on a speci-

*Corresponding author's e-mail:
li.zhifeng@csu.edu.cn

men surface.[17] Jung found that there was a significant decrease in the corrosion resistance of Al with an increase in the concentration of S and temperature.[18] However, all the above researches only focused on the relationship between the corrosion degree of an aluminum alloy and the factors, such as ion concentration, and did not deeply and systematically study the evolution and mechanism of corrosion behavior, which can truly reveal the origin of corrosion and provide understanding required for improving corrosion resistance.

The main purpose of this paper is to reveal the corrosion behavior and the development mechanism of the salt spray corrosion of Al-Si/Al-Mn composites through an artificial salt spray corrosion test.[19,20]

2 EXPERIMENTAL PART

2.1 Materials and sample preparation

The chemical composition of the experimental Al-Si/Al-Mn/Al-Si composite plates is shown in **Table 1**. After being laminated and paired, three-layer alloys were heated to (500 ± 5) °C, hot rolled from (33 + 330 + 33) mm to 7 mm, cold rolled to 1.5 mm and finally annealed at 370 °C for 1 h. Samples of 25 mm × 25 mm were obtained by wire cutting and sealed with insulating glue, keeping an area of 20 mm × 20 mm exposed. Wires were connected to the backs of the samples to facilitate their hanging in the test box. But to avoid the conduction of electricity, the wires were fixed with insulating glue and sealed at both ends.

Table 1: Chemical composition of composite plates (*w*/%)

Alloys	Si	Fe	Mn	Cu	Zn	Al
Al-Mn	0.60	0.70	1.20	0.70	0.10	Bal.
Al-Si	7.00	0.80	0.10	0.25	0.20	Bal.

2.2 Artificial salt spray corrosion test

In order to evaluate the corrosion resistance, a sea water acetic acid test (SWAAT) was carried out in accordance with ASTM G85 on the samples.[21,22] 10 mL of glacial acetic acid and 42 g of NaCl were added to each liter of distilled water, and the pH was adjusted between 2.8 and 3.0 with a NaOH solution. During a continuous 480-h test, the temperature in the exposure zone of the salt spray chamber was set at (49 ± 2) °C and the temperature in the saturator tower was set at (57 ± 1) °C. The spraying method was conducted with 120-min repetitive cycles: 30-min spray and 90-min soak at a relative humidity higher than 98 %. The spray was applied at a rate of 1.0–2.0 mL/h per 80 cm^2 of the horizontal collection area.

2.3 Characterization of the microstructure

Optical metallography (OM), polarized metallography (PM), scanning electron microscopy (SEM), electron probe micro-analysis (EPMA) and X-ray diffraction analysis were applied to explore the morphology and microstructure of the intermetallic compounds and element distribution of the corroded samples after (1, 3, 5, 7, 10, 15 and 20) d during the SWAAT period.

2.4 Corrosion measurements

The electrochemical behavior of the samples corroded during the SWAAT period was investigated after (1, 3, 5, 7, 10, 15 and 20) d, using electrochemical impedance spectroscopy (EIS)[23] via a ZAHNER Im6ex electrochemical workstation. The experimental set-up included a standard three-electrode cell with a platinum sheet as the counter electrode, a KCl-saturated calomel electrode (SCE) immersed in a saturated NaCl solution

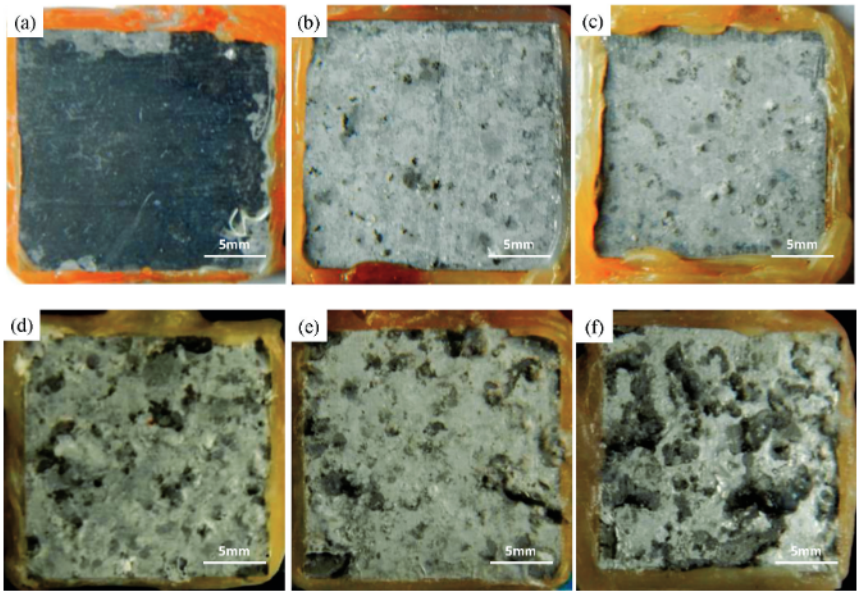

Figure 1: Surface-corroded morphology after: a) 24 h, b) 72 h, c) 120 h, d) 240 h, e) 360 h, f) 480 h

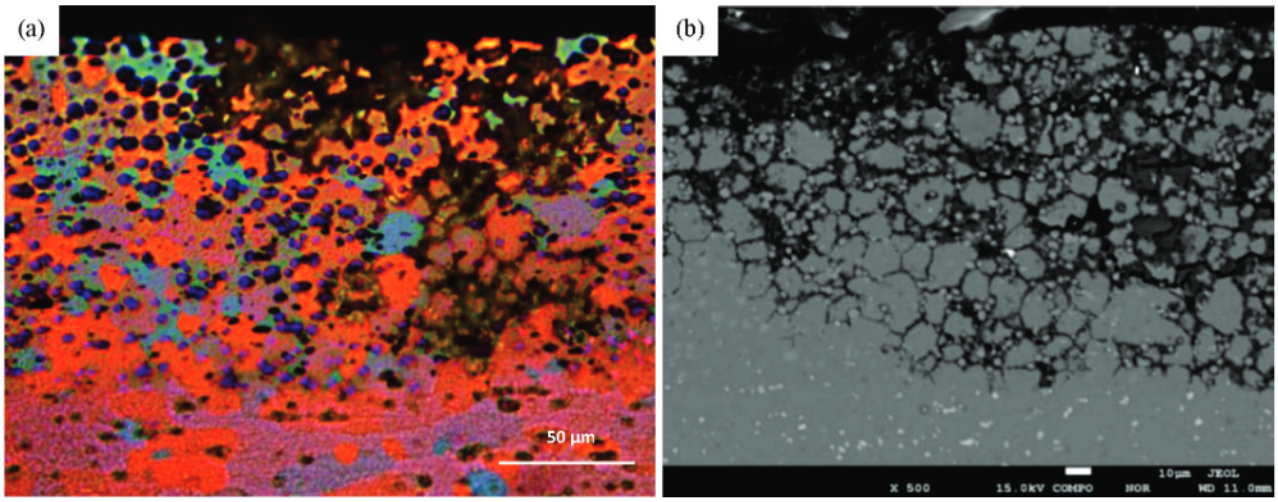

Figure 2: Microstructure of the composite plate after 480-h salt spray: a) optical microscopy, b) SEM

as the reference electrode and a test sample with an exposed area of 20 mm × 20 mm as the working electrode. Moreover, the experimental solution was determined as the SWAAT solution, the amplitude of the disturbance sine wave signal was 20 mV and the frequency ranged from 50 MHz to 100 kHz. The data were analyzed by ZSimpWin software.

3 RESULTS AND DISCUSSION

3.1 Microstructural observation

The surface macro-morphology and the side micro-morphology of the composite plates during salt spray corrosion are shown in **Figure 1**. It can be observed that the surface of the samples was still relatively smooth without obvious signs of corrosion after 24 h of salt spraying. After 72 h, bulges and peelings appeared showing a pitting morphology. After 240 h, the number of pitting holes increased gradually. After 480 h, the surface of the samples peeled off significantly.

Figure 2a shows polarized optical metallographic images of corroded samples after 480 h of salt spraying. Both the filler and the core layer recrystallized completely. The corrosion medium infiltrated along the grain boundaries and sub-grain boundaries of the new grains caused the erosion of the composite plate and even formed cavities on seriously corroded parts. The SEM analysis (**Figure 2b**) clearly showed intergranular corrosion networks where coarse second-phase particles were distributed.

3.2 Intermetallic-particle characterization

In order to explore the causes of the network corrosion, it is necessary to analyze the material structure and composition.

Figure 3 shows the SEM morphology and **Table 2** shows the EPMA analysis results for the cross-section of the Al-Si/Al-Mn composite plate. Additionally, **Figure 4** shows the XRD analysis of the core alloy. The precipi-

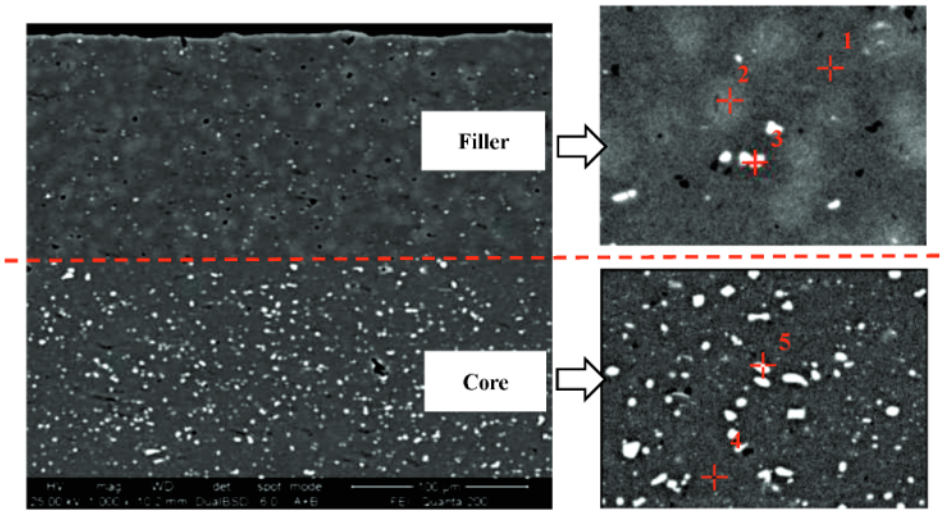

Figure 3: SEM morphology of the Al-Si/Al-Mn composite plate

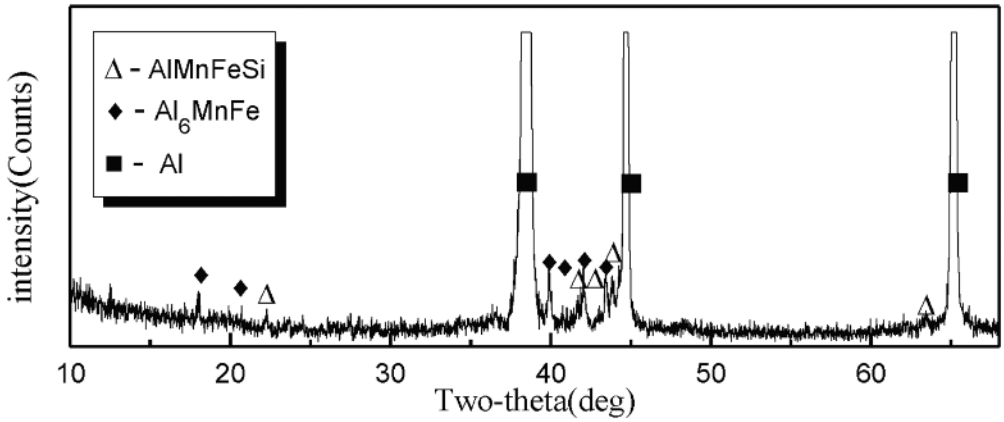

Figure 4: XRD analysis of the core layer

tated phases of the filer were mainly particles rich in silicon (77 *w*/%) and AlSiMnFe phases. The precipitation phases of the core layer were mainly Al_6MnFe and AlMnFeSi phases. It was proven that, as the anode, the potential of the silicon-rich particles is relatively lower than those of the matrix and AlSiMnFe phases, enabling the formation of galvanic cells. The Al-Si/Al-Mn composite structure met these forming conditions to induce corrosion.

Table 2: EPMA analysis of the Al-Si/Al-Mn composite plate (*w*/%)

No.	Si	Mn	Fe	Cu	Zn	Al
1	0.262	0.031	0	0.022	0.077	bal.
2	77.241	0.020	0.106	0.0S22	0.057	bal.
3	28.202	0.055	0.062	0	0.109	bal.
4	0.447	0.569	0.945	0.026	0.131	bal.
5	2.665	8.583	5.934	0.275	0.051	bal.

To analyze the influence of intermetallic compounds on the development of corrosion behavior, the cross-section observation of the salt spray corrosion specimens was intercepted and an EPMA composition analysis was conducted, as shown in **Figure 5** and **Table 3**. The corrosion medium infiltrated along the grain boundaries and sub-grain boundaries of the new grains, and even produced cavities. It could be found that the intergranular corrosion networks were obviously darker than the α(Al) primary crystal. The discontinuous second phases along the corrosion networks were silicon-rich phases. The concentration of oxygen and chlorine in the dark gray area along the corrosion networks was significantly higher than that of the matrix, indicating that the corrosion medium mainly erodes the grain boundaries with chlorine ion.

Table 3: EPMA linear element analysis of salt spray corrosion specimens (*w*/%)

No.	Si	Mn	Fe	Cu	Zn	O	Cl	Al
6	0.401	0.022	0	0.061	0.014	2.471	0.012	bal.
7	0.848	0.090	1.522	0.017	0.223	9.001	0.115	bal.
8	86.638	0.046	0.079	0	0.002	3.887	0.096	bal.

3.3 EIS measurements

To explore the mechanism of the salt spray corrosion development of Al-Si/Al-Mn composites, the corrosion

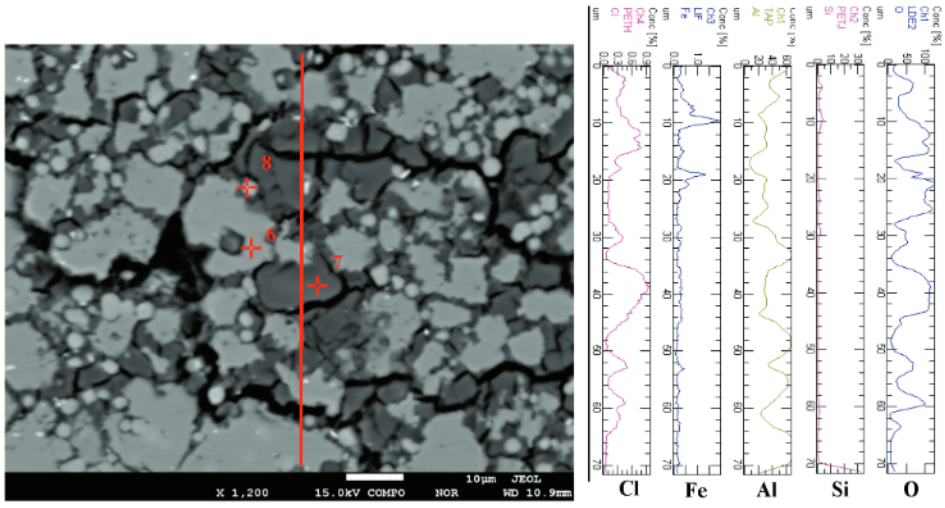

Figure 5: EPMA linear element analysis of a salt spray corrosion specimen (*w*/%)

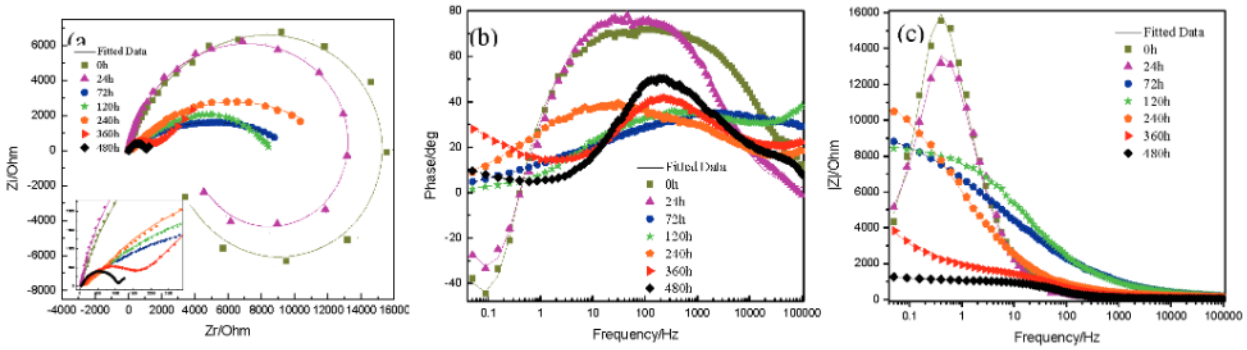

Figure 6: Impedance spectrum of salt spray corrosion for 0–480 h: a) Nyquist diagram, b) Bode phase diagram, c) Bode impedance diagram

behaviors of different corroded samples were dynamically monitored with electrochemical impedance spectroscopy (EIS). The impedance spectrum of salt spray corrosion for 0–480 h is shown in **Figure 6**. Specifically, **Figure 6a** shows the Nyquist diagram, representing the Zr imaginary part of the impedance curve, while **Figure 6b** shows the frequency-phase angle curve of the Bode diagram in logarithmic form, and **Figure 6c** shows the frequency-impedance modulus |Z| curve of the Bode diagram. In each figure, the scatter points are the measured experimental data, and the curves are fitted according to different equivalent circuits.

It can be seen from **Figure 6** that the Nyquist diagram for the corrosion samples for 0–24 h presents a high-frequency capacitance arc and a low-frequency inductance arc. And the frequency-phase curve of the Bode diagram gives two time constants, showing a peak and a valley. The high-frequency capacitance arc is the capacitive arc at the interface between a specimen and the corrosive medium, while the low-frequency inductance indicates that the sample has a surface film layer, and there is a tendency for local corrosion. After being corroded for 72–120 h, in the Nyquist diagrams, the inductance arcs disappear, the capacitance arcs are obviously elongated and flattened, and the real parts of the low-frequency region shrink at the tail. In the meanwhile, in the Bode diagrams, the low-frequency valleys of the frequency-phase curves disappear, and the peak height of the high-frequency region becomes shorter. In addition, two extreme peaks appear gradually, and the tail of |Z| is compressed. All the variations indicate that the corrosive medium penetrated the interior and the specimen could no longer rely on the corrosion resistance of the surface film. After 240 h of corrosion, the radius of the capacitance arc of the Nyquist diagram increases. Meanwhile, the two peaks of the frequency-phase curve move to low frequency, and the tail of |Z| rises, indicating that the corrosive medium is corroded to the substrate and the impedance value of the sample increases. As the corrosion time is extended, the capacitance arcs of the Nyquist diagram gradually shrink, and the tails turn into oblique straight lines at nearly 45°, indicating that the corrosion interface area is sufficient and that corrosion products cannot be accumulated, showing obvious Warburg impedance.

3.4 Developing mechanism of the salt spray corrosion behavior

In order to further verify the microstructure, an equivalent circuit was established with the stages of the EIS data, and the data fitting was carried out using the ZSimpWin software. The fitting error of each parameter was less than 10 %. The corrosion cycle of Al-Si/Al-Mn composites can be divided into the pitting-induction period, pitting-propagation period and matrix-corrosion period.

3.4.1 Pitting-induction period

The R(QR(LR)) equivalent circuit model is used to fit the impedance spectrum of salt spray corrosion during 0–24 h (as shown in **Figure 7**) where R_S is the solution resistance, Q_C is the equivalent leakage capacitance, R_C is the interface reaction resistance, L and R_0 are the

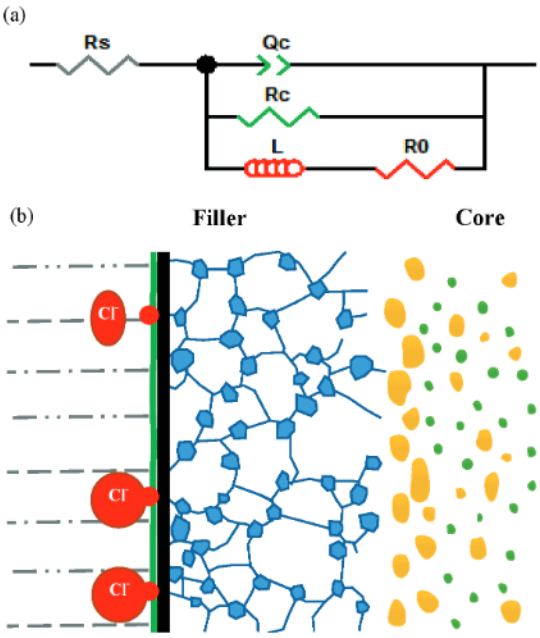

Figure 7: Pitting-induction period: a) equivalent circuit model, b) corrosion-development diagram

Table 4: Fitting parameters of EIS during the pitting-induction period

Corrosion time (h)	R_S/(Ω·cm^2)	Q_C		R_C/(Ω·cm^2)	L/(H·cm^2)	R_0/(Ω·cm^2)
		Y_0/(Ω^{-1}·cm^2·s^{-n})	n			
0	6.451	1.3410^{-5}	0.8124	19240	14530	3516
24	15.51	1.1210^{-5}	0.8833	15310	14990	5459

equivalent inductance and equivalent resistance at the pitting-corrosion active point related to the change in the passive-film thickness or coverage.

The electrode system is not only controlled by the electrode potential, but also affected by the thickness of the film or its coverage. Before salt spray corrosion, the aluminum alloy is easy to be activated in air, and a dense Al_2O_3 film is formed on the surface of the sample, resulting in inductive-reactance components. The oxide film is easy to be dissociated and broken by Cl^- in the corrosive medium, which leads to a decrease in inductive reactance. The Faraday admittance Y_F of the electrode system can be expressed as Equation (1):

$$Y_F = \frac{1}{R_C} + \frac{1}{R_0 + j\omega L} \quad (1)$$

The impedance of the whole electrode system indicates that the Faraday impedance is connected, in parallel, with the interface capacitance Q_C element, and then connected in series with the solution resistance R_S. The Q_C element represents an electrical double-layer capacitor with a dispersion effect in the solid dielectric[24], which is defined as Equation (2):

$$Y_Q = Y_0 (j\omega)^n, \quad 0 < n \leq 1 \quad (2)$$

where n = 1 and Q_C is pure capacitance.

The parameters of the equivalent components are obtained using the model for the 0–24 h corrosion, as shown in **Table 4**, while the fitting errors are all within 10 %. The solution resistance R_S hardly changes with the development of corrosion, having little effect on the electrode system, which can be ignored.

Figure 6 and **Table 4** indicate that with the extension of corrosion time, the interfacial reaction resistance R_C decreases since the rate of formation of chloride, destroying the passive film with the Cl^- adsorption in the corrosive medium on the sample surface is faster than that of absorbing oxygen-containing particles, forming the passive film. With the dissolution of the passive film, the equivalent inductance L and resistance R_0 of the pitting active point first increase and then gradually disappear. Furthermore, the electrode surface becomes rougher, the reaction area increases, the battery reaction increases and the static charge storage capacity of the electric double layer decreases. Therefore, the Y_0 value reflecting the capacitance of the interface Q_C element decreases, while the n value reflecting the dispersion effect of the Q_C element increases with the decrease in the electrode surface roughness and current distribution uniformity.

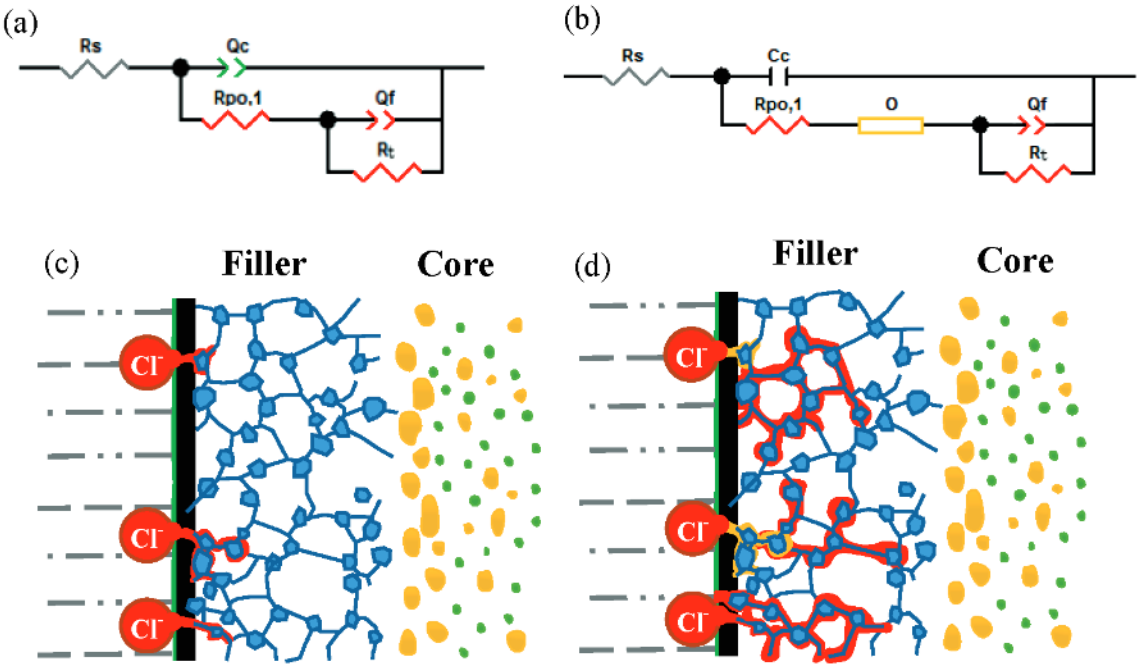

Figure 8: Pitting-propagation period: equivalent circuit model and development diagram: a and c) formation of pitting, b and d) formation of blocking cells

Table 5: Fitting parameters of EIS during pitting-propagation period and matrix-corrosion period

	Corrosion time (h)					
	72	120	240	360	480	
R_S /(Ω·cm^2)	59.12	55.87	83.06	39.97	29.65	
Qc	Y_0 /(Ω^{-1}·cm^{-2}·s^{-n})	1.88×10^{-5}	6.33×10^{-9}	1.18×10^{-8}	3.21×10^{-8}	2.57×10^{-7}
	n	0.447	1	1	1	1
$R_{po,1}$/(Ω·cm^2)	7780	174.7	67.32	43.7	17.25	
O	Y_0 /(Ω^{-1}·cm^{-2}·s^{-5})	–	1.63×10^{-4}	–	–	–
	B/s^{-5}	–	0.1901	–	–	–
Q_f	Y_0/(Ω^{-1}·cm^{-2}·s^{-n})	1.65×10^{-4}	1.40×10^{-5}	4.02×10^{-5}	1.48×10^{-5}	8.96×10^{-6}
	n	0.563	0.5145	0.5147	0.6559	0.7997
$R_{po,2}$/(Ω·cm^2)	–	–	4155	442.3	266.2	
W/(Ω^{-1}·cm^{-2}·s^{-5})	–	–	–	0.000699	0.005834	
C_a/F	–	–	9.79×10^{-7}	6.52×10^{-7}	1.61×10^{-6}	
R_t /(Ω·cm^2)	1910	7411	8576	1124	722	

3.4.2 Pitting-propagation period

The $R(Q(R(QR)))$ equivalent circuit model is used to fit the impedance spectrum of salt spray corrosion after the corrosion of 72 h as shown in **Figures 8a** and **8c** where R_S is the solution resistance, Q_C is the equivalent leakage capacitance at the interface, $R_{po,1}$ is the solution resistance (i.e., pore resistance), Q_f and R_t are the constant phase angle and charge transfer reaction resistance of the interface reaction in the pores of cortical corrosion, respectively. During this period, the electrode reaction not only occurs on the passive film, but also invades the sub-surface to form corrosion holes. The transfer resistance of the passive film is very large and the admittance can be ignored.

The parameters of the equivalent components are obtained as shown in **Table 5**. From their combination with the impedance spectrum from **Figure 6**, it can be seen that the corrosion pores are small and there is no obvious medium diffusion in the early stage. With the further development of corrosion, the corrosive medium obviously diffuses into the interface of the pores, while the corrosion products can hardly discharge out smoothly in the narrow pores and accumulate in the pores to form closed cells, limiting the diffusion process to length-constrained diffusion. Therefore, the O element should be added to represent the influence of cell blocking on the diffusion process. The admittance of the O element is defined as Equation (3):

$$Y_O = Y_0 (j\omega)^{1/2} \coth\left[B(j\omega)^{1/2}\right] \quad (3)$$

where coth is the hyperbolic cotangent function.

Then the $R(Q(RO(QR)))$ model should be used to fit the corrosion after 120 h as shown in **Figures 8b** and **8d**. The roughness and current distribution of the interface between a sample and the corrosive medium are weakened, but the capacity of charge carrying continues to decline and the Q_C element finally changes into pure capacitance C_C. The diffusion becomes more obvious, but it should be weakened with the increase in the corrosion-pore size. With the increase in the surface roughness, the corrosion-product coverage, the depth of corrosion hole and the decrease in the effective interface-medium reaction area, the Y_0 and n value of the constant phase-angle element Q_f decrease gradually and the charge transfer resistance R_t increases significantly.

3.4.3 Matrix-corrosion period

With the pitting-hole deepening, the corrosive medium penetrates the filler and begins to penetrate the matrix after 240 h of salt spray corrosion. As shown in **Figures 9a** and **9c**, the appropriate circuit model is changed to $R\ (C(R(Q(R(CR)))))$ where R_S is still the solution resistance, C_C is the interface capacitance, $R_{po,1}$ is the surface-pore resistance, Q_f is the constant phase-angle element of the interface reaction in the surface pores, $R_{po,2}$ is the deep-pore resistance in the matrix, C_a and R_t are the interface capacitance and charge-transfer resistance between the anodic dissolved metal in deep pores and the corrosive medium, respectively.

From the combination of the impedance spectrum from **Figure 6** and fitted parameters from **Table 5**, it can be seen that after the corrosive medium invades the matrix, the transfer resistance R_t increases, the capacitance arc of impedance spectrum increases, the tail of |Z| increases, the double peak splitting phenomenon of the phase angle is more obvious and the two peaks move to low frequency.

With the increasing and deepening of pitting holes, the corrosion products increase, causing only limited hindrance to diffusion since a corrosion hole is wide at the top and narrow at the bottom. The Warburg element is introduced to describe this half-infinite-length impedance, and the $R(C(R(Q(RW(CR)))))$ model is used for fitting, as shown in **Figures 9b** and **9d**.

With the anodic sacrificial dissolution strengthening in the deep pores, the medium exchange is accelerated, R_t, $R_{po,1}$, $R_{po,2}$ gradually decrease, and W gradually increases. The roughness of the interface between the metal and corrosive medium decreases, while the corrosive current increases and the uneven distribution weakens, leading to a decrease in Q_f and C_a. With the increase

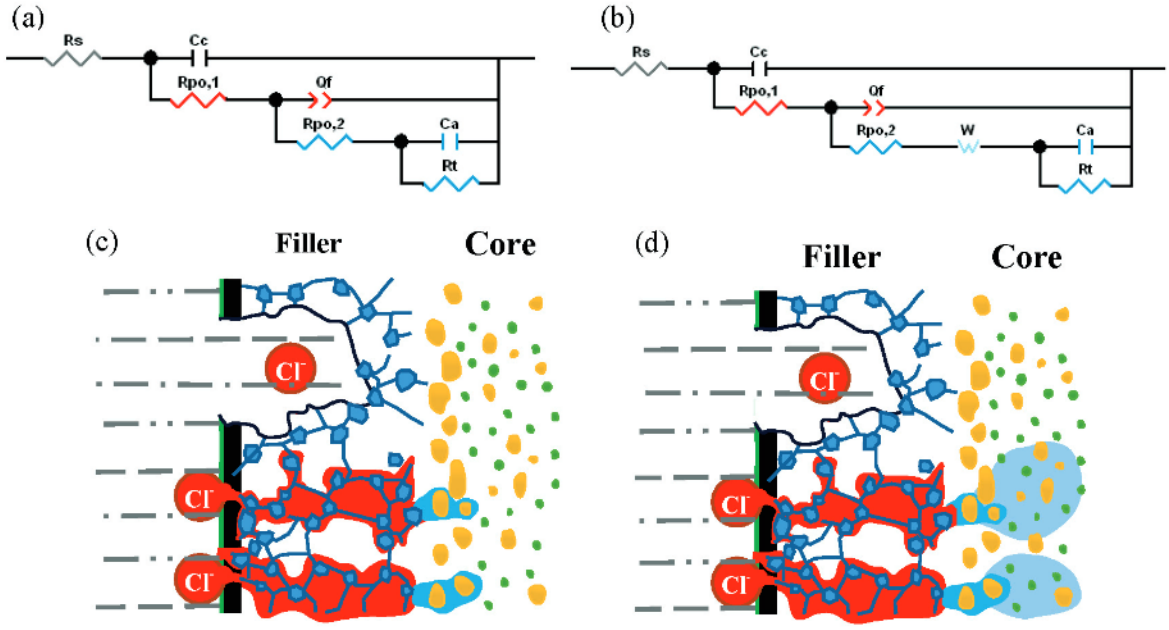

Figure 9: Matrix-corrosion period: equivalent circuit model and development diagram: a and c) initial stage of matrix corrosion, b and d) diffusion enhancement

in the corrosion time, the whole impedance spectrum shrinks greatly, the impedance modulus |Z| increases and the electrochemical corrosion reaction of the system becomes more severe.

4 CONCLUSIONS

Two interaction mechanisms occur in Al-Si/Al-Mn composites during salt spraying: pitting corrosion and intergranular corrosion. In salt spraying, Cl^- in the corrosive medium preferentially adsorbs on the active points such as defects, destroys the passive film with a chemical reaction and induces pitting corrosion. The corrosive medium in pitting holes develops along the grain boundaries, where phases rich in Si are enriched, and corrodes the anodic eutectic α (Al).

The electrochemical corrosion process of Al-Si/Al-Mn composites in a salt-spray environment includes the pitting-induction period, pitting-propagation period and matrix-corrosion period. In the pitting-induction period, the passive film on the surface is destroyed by absorbing Cl^- in the corrosive medium and the fitting equivalent circuit is the $R(QR(LR))$ model. In the pitting-propagation period, the corrosive medium invades the interior of the composite plate to form corrosion holes, and the equivalent circuit is first $R(Q(R(QR)))$ but then, with the coarsening of the surface, the deepening of the corrosion holes and the accumulation of products, the equivalent circuit changes to $R(CO(QR)))$. In the matrix-corrosion period, the corrosive medium penetrates the matrix and the equivalent circuit is first $R(C(R(Q(R(CR)))))$ and finally, with the increase in diffusion, it becomes $R(C(R(Q(RW(CR)))))$.

Acknowledgement

This research was financially supported by the Fundamental Research Funds for the Central Universities of the Central South University (Granted No. 2018zzts020).

5 REFERENCES

[1] M. J. Benoit, H. Jin, B. Shalchi-Amirkhiz, S. Kurukuri, S. Winkler, M. J. Worswick, M. A. Wells, Microstructure evolution of warm deformed multilayered Al alloy sheet during brazing, J. Mater. Process. Technol., 281 (**2020**), 116639, doi:10.1016/j.jmatprotec.2020.116639

[2] S. T. W. Kuruneru, K. Vafai, E. Sauret, Y. Gu, Application of porous metal foam heat exchangers and the implications of particulate fouling for energy-intensive industries, Chem. Eng. Sci., 228 (**2020**), 115968, doi:10.1016/j.ces.2020.115968

[3] H. Rastan, A. Abdi, B. Hamawandi, M. Ignatowicz, J. P. Meyer, B. Palm, Heat transfer study of enhanced additively manufactured minichannel heat exchangers, Int. J. Heat Mass Transfer, 161 (**2020**), 120271, doi:10.1016/j.ijheatmasstransfer.2020.120271

[4] P. Oclon, P. Cisek, E. Kozak-Jagiela, J. Taler, D. Taler, D. Skrzyniowska, M. Fedorczak-Cisak, Modeling and experimental validation and thermal performance assessment of a sun-tracked and cooled PVT system under low solar irradiation, Energy Convers. Manage., 222 (**2020**), 113289, doi:10.1016/j.enconman.2020.113289

[5] H. Güllüce, K. Özdemir, Design and operational condition optimization of a rotary regenerative heat exchanger, Appl. Therm. Eng., 177 (**2020**), 115341, doi:10.1016/j.applthermaleng.2020.115341

[6] M. Bezaatpour, H. Rostamzadeh, J. Bezaatpour, M. Ebadollahi, Magnetic-induced nanoparticles and rotary tubes for energetic and exergetic performance improvement of compact heat exchangers, Powder Technol., 377 (**2021**), 396–414, doi:10.1016/j.powtec.2020.09.010

[7] F. C. Alverson, M. Ranger, H. J. DeBaun, The Effects of Residual Controlled Atmospheric Brazing Flux on Engine Coolants, Global Testing of Extended Service Engine Coolants and Related Fluids, 1556 (**2014**), 175–194, doi:10.1520/stp155620130067

[8] A. Akbari, S. Kouravand, S. Pourahmad, A comprehensive study of the second law of thermodynamics for a rotary regenerative heat

exchanger with two types of simple and anodized aluminum sheets: an experimental study, Energy Sources, Part A: Recovery, Utilization and Environmental Effects, (**2020**), 1–16, doi:10.1080/15567036.2020.1771479

[9] E. Emmons, P. J. Shamberger, Corrosive effect of lithium nitrate trihydrate on common heat exchanger materials, Materials and Corrosion – Werkstoffe und Korrosion, 70 (**2019**) 5, 877–887, doi:10.1002/maco.201810557

[10] L. Jackowski, P. Risse, R. Smith, Impact of Nonuniform Fouling on Operating Temperatures in Heat Exchanger Networks, Heat Transfer Engineering, 38 (**2017**) 7–8, 753–761, doi:10.1080/01457632.2016.1206417

[11] L. Bialo, T. Grodniewicz, P. Zabinski, Selected cyclic corrosion tests in automotive industry, Archives of Metallurgy and Materials, 65 (**2020**) 4, 1469–1476, doi:10.24425/amm.2020.133715

[12] K. Chandra, V. Kain, S. K. Sinha, H. G. Gujar, Metallurgical investigation of a heat-exchanger tube of 70/30 cupronickel failed by fretting corrosion, Engineering Failure Analysis, 116 (**2020**), 104756, doi:10.1016/j.engfailanal.2020.104756

[13] H. Peltola, M. Lindgren, Failure analysis of a copper tube in a finned heat exchanger, Engineering Failure Analysis, 51 (**2015**), 83–97, doi:10.1016/j.engfailanal.2015.02.016

[14] S. Nasrazadani, S. Nakka, Characterization of Corrosion Products in RTPF and All-Aluminum Microchannel Heat Exchangers, Journal of Failure Analysis and Prevention, 16 (**2016**) 2, 189–196, doi:10.1007/s11668-016-0078-1

[15] Y. S. Kim, I. J. Park, J. G. Kim, Simulation Approach for Cathodic Protection Prediction of Aluminum Fin-Tube Heat Exchanger Using Boundary Element Method, Metals, 9 (**2019**) 3, 376, doi:10.3390/met9030376

[16] J. Su, M. Ma, T. Wang, X. Guo, L. Hou, Z. Wang, Fouling corrosion in aluminum heat exchangers, Chinese Journal of Aeronautics, 28 (**2015**) 3, 954–960, doi:10.1016/j.cja.2015.02.015

[17] S. Y. Cho, J. J. Kim, H. J. Jang, Effects of Zn Coating and Heat Treatment on the Corrosion of Aluminum Heat Exchanger Tubes, Corrosion Science and Technology - Korea, 18 (**2019**) 1, 24–32, doi:10.14773/cst.2019.18.1.24

[18] J. Jung, S. Oh, H. Kwon, Effects of environmental factors on corrosion behavior of aluminum, Materials and Corrosion - Werkstoffe und Korrosion, 72 (**2020**) 3, 557–563, doi:10.1002/maco.202011676

[19] S. Kumar, H. Singh, N. Gaur, S. Patil, D. Kumar, N. Singh, Imparting increased corrosion passive and bio-active character to Al_2O_3 based ceramic coating on AZ91 alloy, Surface and Coatings Technology, 383 (**2020**), 8, doi:10.1016/j.surfcoat.2019.125231

[20] T. T. Thai, A. T. Trinh, G. V. Pham, T. T. T. Pham, H. N. Xuan, Corrosion Protection Properties of Cobalt Salt for Water-Based Epoxy Coatings on 2024-T3 Aluminum Alloy, Corrosion Science and Technology - Korea, 19 (**2020**) 1, 8–15, doi:10.14773/cst.2020.19.1.8

[21] B. Leszczynska-Madej, M. Richert, A. Wasik, A. Szafron, Analysis of the Microstructure and Selected Properties of the Aluminium Alloys Used in Automotive Air-Conditioning Systems, Metals, 8 (**2018**) 1, 15, doi:10.3390/met8010010

[22] R. M. Katona, S. Tokuda, J. Perry, R. G. Kelly, Design, construction, and validation for in-situ water layer thickness determination during accelerated corrosion testing, Corros. Sci., 175 (**2020**), 108849, doi:10.1016/j.corsci.2020.108849.24

[23] F. Ciucci, Modeling electrochemical impedance spectroscopy, Current Opinion in Electrochemistry, 13 (**2019**), 132–139, doi:10.1016/j.coelec.2018.12.003

[24] Z. Lukacs, T. Kristof, A generalized model of the equivalent circuits in the electrochemical impedance spectroscopy, Electrochim. Acta, 363 (**2020**), 137199, doi:10.1016/j.electacta.2020.137199